

---

# Gradient strikes back: How filtering out high frequencies improves explanations

---

Sabine Muzellec<sup>\*,1,2</sup>, Léo Andéol<sup>\*,3,4</sup>, Thomas Fel<sup>\*,1,4</sup>,  
Rufin VanRullen<sup>2</sup>, Thomas Serre<sup>1</sup>,

<sup>1</sup>Carney Institute for Brain Science, Brown University, USA

<sup>2</sup>CerCo, CNRS, France

<sup>3</sup>Institute of Mathematics of Toulouse, University Paul Sabatier, France

<sup>4</sup>SNCF, France

{sabine\_muzellec, thomas\_fel}@brown.edu, leo.andeol@math.univ-toulouse.fr

## Abstract

Recent years have witnessed an explosion in the development of novel prediction-based attribution methods, which have slowly been supplanting older gradient-based methods to explain the decisions of deep neural networks. However, it is still not clear why prediction-based methods outperform gradient-based ones. Here, we start with an empirical observation: these two approaches yield attribution maps with very different power spectra, with gradient-based methods revealing more high-frequency content than prediction-based methods. This observation raises multiple questions: What is the source of this high-frequency information, and does it truly reflect decisions made by the system? Lastly, why would the absence of high-frequency information in prediction-based methods yield better explainability scores along multiple metrics? We analyze the gradient of three representative visual classification models and observe that it contains noisy information emanating from high-frequencies. Furthermore, our analysis reveals that the operations used in Convolutional Neural Networks (CNNs) for downsampling appear to be a significant source of this high-frequency content – suggesting aliasing as a possible underlying basis. We then apply an optimal low-pass filter for attribution maps and demonstrate that it improves gradient-based attribution methods. We show that *(i)* removing high-frequency noise yields significant improvements in the explainability scores obtained with gradient-based methods across multiple models – leading to *(ii)* a novel ranking of state-of-the-art methods with gradient-based methods at the top. We believe that our results will spur renewed interest in simpler and computationally more efficient gradient-based methods for explainability.

## 1 Introduction

Explaining and interpreting the decision of AI architectures is an important area of research towards enabling the development of more interpretable models [1–3]. Explainability methods (XAI) aim to provide insights into the strategies used by models to arrive at their decision. This is expected to lead to the development of better models that are more accurate, robust, and better aligned with humans. One of the first attribution methods proposed, “Saliency” [4], consists of back-propagating a model’s decision back to an input image to highlight areas that most affected the final decision. The method remains relatively simple and computationally efficient, but it is also known to be noisy and to lead to

---

\* The authors contributed equally.

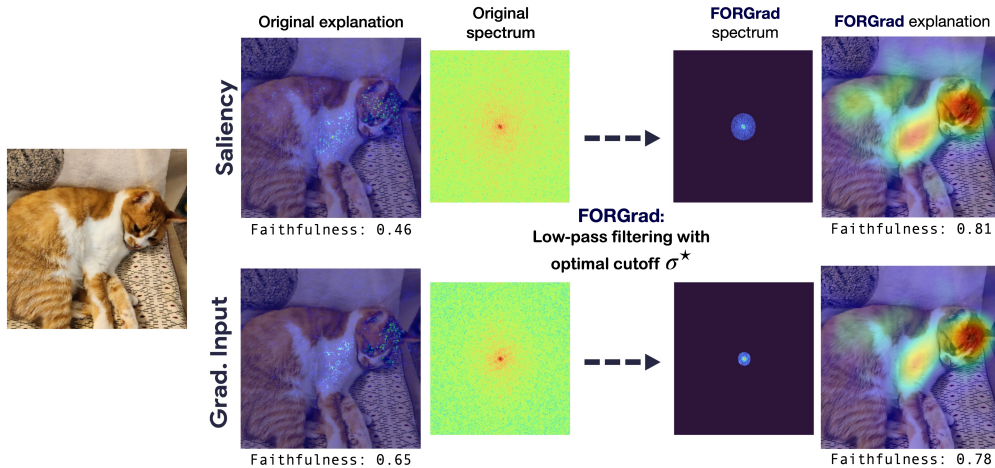


Figure 1: **Effect of FORGrad on gradient-based attribution methods.** We show that for an input image (left), the initial explanations from two gradient-based methods are plagued by noise as indicated by the high power in the high-frequency range of their respective spectra. Filtering the explanations with **FORGrad** yields improved explanations (right).

attribution maps that are often hard to interpret. Multiple methods have been proposed since to try to improve on these limitations. These methods fall broadly into two main classes. (i) Gradient-based methods extend Saliency [4] to build more sophisticated importance estimators [5–12]. However, these so-called white-box methods require access to all the model’s components, which is not always possible. Conversely, prediction-based methods, also called black-box methods [6, 13–16], alter the input of the model to produce an explanation based on the resulting change in the output. Those methods are computationally inefficient and are known to sometimes fail to capture all the diagnostic information, but they currently lead to the best fidelity scores across all explainability methods. Overall, there have been relatively few notable studies that have delved into the intricacies of attribution methods [17–23]. Hence, the factors that determine the superior performance of certain methods over others remain relatively unclear.

Here, we start with the observation made across multiple studies [24, 7, 25, 26, 18, 27–29] that the attribution maps derived with Saliency are very noisy. Generally, these maps highlight sparse pixel activations around a region of interest, and they are often hard to interpret [30–34]. Because Saliency is simply the gradient of the score function with respect to the input, we suggest that the noise originates from the gradient itself: in other words, because the gradient is noisy, the explanation provided by Saliency is also noisy. To try to better understand the origin of this noise, we compare the Fourier power spectra of gradient-based methods (including Saliency) against prediction-based methods and observe that they differ quite markedly. We discern significant differences between the two classes of approaches, with gradient-based methods returning higher frequency content and prediction-based methods returning lower frequency content. In the remainder of this paper, we will show that:

- The gradient is indeed noisy, and this noise is especially present in the high-frequencies.
- We then look for the origin of these high frequencies in vision models. Our findings show that downsampling operations (via MaxPooling or strides) are the main sources of high frequencies, and training the model does not alleviate the issue.
- We then propose to repair Saliency – as well as other gradient-based methods – by introducing **FORGrad** (FOurier REparation of the GRAdient). This method consists in estimating the optimal amount of high frequencies to remove per model to make gradient-based methods surpass the prediction-based family of attribution methods.

## 2 Related Work

**Attribution methods for black-box models** Various methods have been developed to compute importance scores for individual pixels or groups of pixels. For black-box (prediction-based) attribution methods, the analytical form and potential internal states of the model are unknown. The

first method, Occlusion [6], masks individual image regions, one at a time, using an occluding mask set to a baseline value. The corresponding prediction scores are assigned to all pixels within the occluded region, providing an easily interpretable explanation. However, occlusion as a standalone method falls short in capturing the (higher-order) interactions among various image regions – also called coalitions [35]. For instance, occluding two image regions individually may only have a minimal impact on the model’s prediction, such as removing a single eye or mouth component from a face. However, occluding these two regions together may lead to a substantial change in the model’s prediction if these regions interact non-linearly, as expected in a deep neural network. Sobol [14], along with related methods such as LIME [15] and RISE [13], address this problem by randomly perturbing multiple regions of the input image simultaneously. Interestingly, recent studies, including RISE [13] Sobol [14] and HSIC [16], have demonstrated that black-box attribution methods can rival and even surpass the commonly used white-box methods without relying on internal states.

**Attribution methods for white-box models** The gradient-based methods, that we propose to improve here, were first introduced in [36] and improved in [5–7]. They consist in explaining the decisions of a model by back-propagating the gradient from the output to the input, indicating which pixels affect the decision score the most. However, this family of methods is limited because they focus on the influence of individual pixels in an infinitesimal neighborhood in the input image. For instance, it has been shown that gradients often vanish when the prediction score to be explained is near the maximum value [9]. Integrated Gradient [9] and SmoothGrad [8] partially address this issue by accumulating gradients. Another family of attribution methods relies on the neural network’s activation, like CAM [10], which computes an attribution score based on a weighted sum of feature channel activities – right before the classification layer. GradCAM [11] extends CAM via the use of gradients, re-weighting each feature channel to take into account their importance for the predicted class. Nevertheless, the choice of the layer has a huge impact on the quality of the explanation. Our contribution proposes to overcome some of the mentioned issues by removing the noise present in the gradients in the form of high frequencies.

**Fourier analysis of vision models** Very little work has been proposed to analyze vision models and methods from a Fourier perspective. The closest, [37], used Fourier analysis to investigate the impact of DNNs optimization parameters and methods without a specific focus on vision. Additional work has focused on the analysis and development of adversarial attacks in the Fourier domain, [38, 39], while others [40–42] have proposed to defend against adversarial attacks by transforming the input image in the Fourier domain. Jo and Bengio [43] examined whether CNNs rely on high-level features by using Fourier-filtered images. None of the mentioned studies make a link between explainability and attribution methods with Fourier analysis.

### 3 Decomposing the gradient: An analysis of frequency content in attribution methods

**Notations** We consider a general supervised learning setting, where a classifier  $f : \mathcal{X} \rightarrow \mathcal{Y}$  maps images from an input space  $\mathcal{X} \subseteq \mathbb{R}^{W \times H}$  to an output space  $\mathcal{Y} \subseteq \mathbb{R}$ . Let  $(\mathbf{x}_1, \dots, \mathbf{x}_N)$  be a set of images which contains  $N$  samples drawn from a probability distribution  $\forall i \in \{1 \dots n\}, \mathbf{x}_i \sim \mathcal{D}$ . Moreover, we respectively denote  $\mathcal{F}$  and  $\mathcal{F}^{-1}$  the Discrete Fourier Transform (DFT) on  $\mathbb{R}^{W \times H}$  and its inverse. Therefore:  $\forall \mathbf{x} \in \mathcal{X}, \mathcal{F}(\mathbf{x}) \in \mathbb{C}^{W \times H}$  and  $(\mathcal{F}^{-1} \circ \mathcal{F})(\mathbf{x}) = \mathbf{x}$ . Additionally, when we visualize the Fourier spectrum, we always shift the low-frequency components to the center of the spectrum. We recall that an attribution method is a function  $\varphi : \mathcal{X} \rightarrow \mathbb{R}^{W \times H}$  that maps an input of interest to its corresponding importance scores  $\varphi(\mathbf{x})$ . Finally, we denote by  $\varphi_\sigma(\mathbf{x})$  the attribution method where high frequencies have been filtered using a cutoff value of  $\sigma$ .

#### 3.1 Different signatures for different categories of methods

In this work, we analyze the Fourier signature of several attribution methods. To do so, we compute the feature map  $\varphi(\mathbf{x})$  for most existing attribution methods on representative models of the literature (ResNet50 in Figure 2). From these importance maps, we extract the corresponding amplitude of the Fourier spectrum,  $|(\mathcal{F} \circ \varphi)(\mathbf{x})|$ . In Figure 2, we show the average power spectra, over 1,000 images, for an array of methods. Upon visual inspection, it is obvious that certain methods tend to emphasize higher frequencies in their explanations, while others concentrate on lower frequencies. Interestingly, these differences can be traced to the class of methods: Black-box methods, which do not rely on gradients, exhibit frequency footprints dominated by very low frequencies, whereas white-box methods exhibit footprints that extend into higher frequencies. To quantify our observations, we

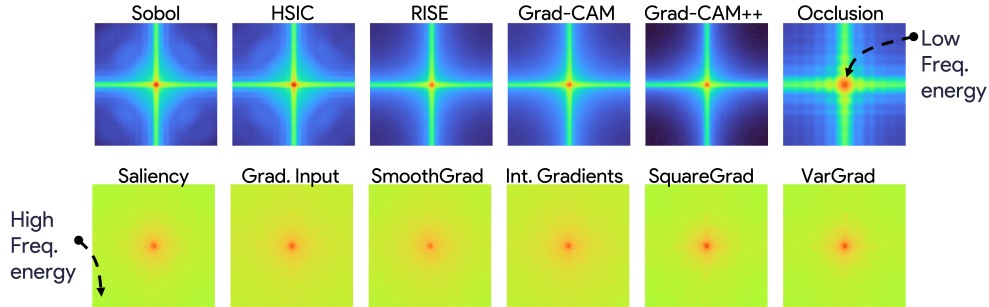


Figure 2: **Fourier footprint of attribution methods.** We show on the top row the Fourier spectrum of prediction-based attribution methods and of the gradient-based methods on the bottom row, computed with a ResNet50. The two families can be distinguished by methods but also by their signature in the Fourier domain. The former method has magnitudes largely concentrated in the low frequencies, while the latter is more spread out: it features non-trivial magnitudes almost everywhere, including in high frequencies.

employ two metrics to measure the complexity of the attribution maps. The first metric employs a Laplacian-based operator [44, 45] that evaluates the presence of high frequencies in images by analyzing their second derivative. The second metric involves measuring the file size of the image after undergoing lossless compression [46, 47], which we refer to as “High-frequency content” throughout this study (as it can be seen as a loose approximation of Kolmogorov complexity). Both metrics validate our visual observations, as depicted in Figure 3 (see Laplace quantity in appendix). It is evident that black-box methods (shown in dark in the figure) exhibit fewer high frequencies compared to white-box methods. This observation provides valuable insight into where these methods extract information from the model to compute their explanations.

### 3.2 High-frequencies are just noise in the gradient

Naturally, gradient-based methods will be subject to the characteristics of the gradient itself. Consequently, when the gradient is subject to noise, the resulting explanation provided by such methods becomes similarly noisy. In light of this observation, we propose to demonstrate that the gradients obtained from three state-of-the-art models (ResNet50 [48], ViT [49], and ConvNeXT [50]) do indeed contain noise, predominantly present in high-frequency components. To achieve this, we suggest an approach that involves selectively removing high-frequency gradient information by employing various frequency cutoffs  $\sigma$ . By computing residuals between  $f(x + \varepsilon)$  and its first order filtered by  $\sigma$  decomposition around  $x$  that we denote by  $f(x) + \varepsilon \nabla_x^\sigma f(x)$ , we generate corresponding curves for different scales of  $\varepsilon$ , which are presented in Figure 4. As anticipated, our observations reveal that the curves exhibiting reduced high-frequency content (from  $\sigma < 224$  to  $\sigma = 10$ ) closely align with the one of the non-filtered gradient ( $\sigma = 224$ ). In other words, the gradient remains approximately as informative, even after removing high-frequency information. This implies that the high-frequency content primarily contains noisy information within the gradient.

### 3.3 Investigating the mechanisms introducing noise

Next, we investigated the underlying operations responsible for the introduction of such content by computing the power of high-frequency content in the gradients at the level of all the layers. Notably, we observed a consistent trend in CNNs where high-frequency content tends to increase and jump at each block, indicative of downsampling operation through strided convolutions or pooling. This observation aligns with the findings of [51, 52], suggesting that downsampling

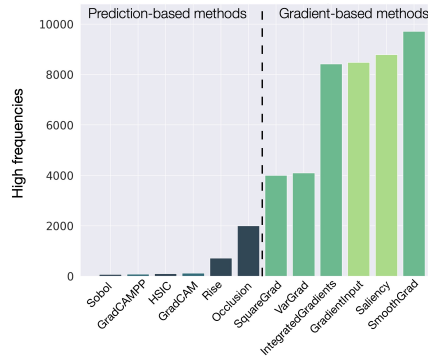


Figure 3: **High-frequency power in attribution methods.** High-frequency power present in the importance maps derived from different attribution methods. Prediction-based methods produce less high-frequency content than gradient-based methods.



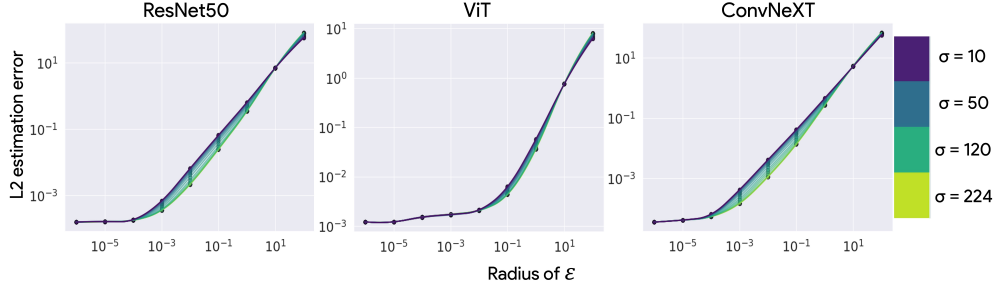


Figure 4: **Evidence for noise in the gradient.** We plot the residual of the first-order approximation of the model, that is  $f(x + \varepsilon) \approx f(x) + \varepsilon \nabla_x f(x)$ , with the gradient  $\nabla f$  filtered at different bandwidths  $\sigma$ . We sample 100 values of  $\varepsilon$  uniformly on  $\mathbb{S}_{d-1}$  scaled by the radius, for 1,000 images of the validation set of ImageNet. If high-frequencies contained information necessary for a good linearization of the model then we would observe a gap between the curves of  $\sigma = 224$  - where no filter is applied, vs. the curves where we apply a filter -  $\sigma < 224$ .

operations via MaxPooling or strided convolution can introduce noise. To verify this hypothesis, we substituted these specific operations in two representative CNNs, namely ResNet50 [48] (which incorporates strided convolutions and MaxPooling) and VGG16 [53] (details in appendix) with AveragePooling. This replacement ensured the preservation of information continuity in the gradient. The resulting plots for ResNet50 (VGG) are presented in Figures 5 - bottom curve (see appendix for VGG), displaying the power of high-frequency content using Kolmogorov image compression and Laplace-operator (see appendix) at each step. The depicted red shades represent the amount of high-frequency content in both models. We observe that prior to the initial dimension change, the quantity of high-frequency content remain comparable, suggesting that operations within a block of the same dimension does not significantly increase the power of high-frequency content. However, with the introduction of a downsampling layer, the curves for each model diverge, indicating a bigger contribution to the introduction of high frequencies by striding or MaxPooling compared to AveragePooling. Our findings corroborate the observations of [51], as the gradients (even averaged) following MaxPooling or strides exhibit checkerboard patterns, providing a plausible explanation for our quantitative observation of increased high-frequency content.

We employ the same pipeline to calculate the high-frequency content for both a random model and a trained model, using the identical set of models including ViT [49]. The resulting curves are depicted in Figures 5 - top curve, for ResNet50 (see appendix for VGG16 and for ViT), showcasing that there is no discrepancy in high-frequency content between the trained and random CNNs. Given our previous section’s demonstration that high-frequencies carry negligible information for the model, one would expect that training could potentially eliminate this content, leaving only relevant information to be processed. However, as our observations indicate the absence of such behavior despite the models accomplishing the task, we propose that the models were unable to adapt the gradient’s content, thereby suggesting it to be an inherent by-product of downsampling operations. In the case of the ViT, however, training appears to introduce some high frequencies from the initial operation, potentially arising from transformers’ pre-processing functions, such as image flattening via patches. These multiple findings suggest that high-frequency content emerges as a by-product of particular operations, predominantly observed in CNNs, which the models are unable to modulate during training. We therefore propose to consider most of the high-frequency content as noise. Consequently, when generating explanations for the models’ decisions, it is justifiable to disregard high frequencies as they offer limited or negligible information.

### 3.4 FORGrad: a simple strategy to remove noise

**An adapted  $\sigma^*$  per model** With FORGrad, we propose to remove high-frequency content, considered as noise, in order to obtain an optimal explanation related to the optimal frequency band from the gradient. We therefore propose to apply a low-pass filter on the Fourier spectrum of the gradient, employing multiple frequency cutoffs spaced evenly apart. For each filtered explanation, we compute the score from two different metrics. The first one Deletion – denoted  $D(\varphi(x))$  [13] – is a measure of the decrease in the likelihood of a particular class as the important pixels (identified by the saliency map) are systematically removed from the image. If the likelihood of the class

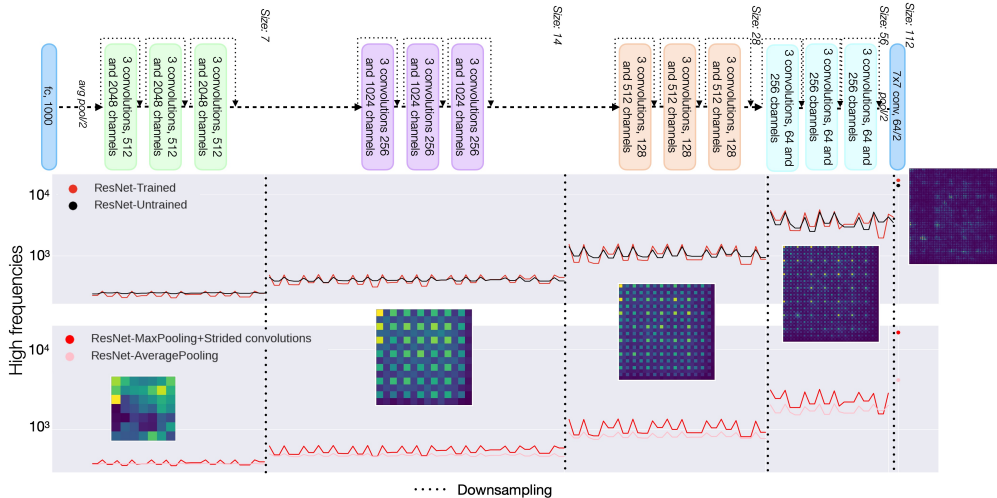


Figure 5: **Evolution of the high-frequency content in Resnet50.** We compute the high-frequency content along the depth of a ResNet50 varying either the weights or the pooling. The top curve represents the trained model, indicated by the red curve, while the untrained model is represented by the black curve. The bottom curve illustrates the impact of different poolings, with MaxPooling and stride shown in dark red and AveragePooling in pink. Each point on the graph corresponds to a layer within the models. In addition, we present visual examples of averaged gradients across 128 images after applying MaxPooling. Despite the averaging process, these examples exhibit checkerboard patterns, serving as a visual demonstration of the presence of high-frequencies.

experiences a rapid decrease, resulting in a small area under the probability curve, this is a strong indication of a good explanation. Complementary, Insertion,  $I(\varphi(x))$  [13] measures the significance of the pixels based on their capacity to create an image, and is calculated by measuring the increase in the probability of the class of interest as pixels are added in accordance with the generated importance map. Overall, we propose a heuristic to optimize our  $\sigma^*$ , representing the ideal bandwidth maximizing the difference  $\sigma^* = \arg \max_{\sigma} \mathbb{E}_x D(\varphi_{\sigma}(x)) - I(\varphi_{\sigma}(x))$ , combining the score of both metrics, on a subset of the validation set of ImageNet (1,000 images). Using both deletion and insertion metrics can provide a more comprehensive evaluation of the quality of the attribution map or saliency map generated for a given model. The deletion metric is useful for identifying important regions of an image that contribute to a model’s decision, while the insertion metric is valuable for assessing the quality of the generated saliency map in terms of its ability to reconstruct the original image. By combining both metrics, we aim to assess the quality of the explanations generated by considering the impact of pixel removal and addition on the likelihood and significance of the target class, respectively. In the latter sections, we will consider the faithfulness metric to be the combination [Deletion-Insertion] Additionally, we also evaluate **FORGrad** on a third metric, MuFidelity,  $F(\varphi(x))$ , [54]. The fidelity correlation metric serves to verify the correlation between the attribution score and a random subset of pixels. To achieve this, a set of pixels is randomly chosen and set to a baseline state, after which a prediction score is obtained. The fidelity correlation metric evaluates the correlation between the decrease in the score and the significance of the explanation for each random subset created.

**Theoretical foundations** In this section, we build on the empirically demonstrated assumption that the gradient is noisy and prove, through a Fourier perspective, that **FORGrad** effectively recovers the true gradient. Moreover, assuming that the noise is originally Gaussian, we characterize the distribution of the noise in Fourier space. Finally, we propose a convergence bound for SmoothGrad, valid on finite samples, showing that it also recovers the true gradient at the cost of multiple samplings.

We denote  $\|\cdot\|_F$  as the Frobenius norm and  $\|\cdot\|_2$  as the spectral norm. Note that  $\|\cdot\|_2 \leq \|\cdot\|_F$  in order to interpret our results. Finally, we define  $\mathbf{K}^{\sigma} \in \{0, 1\}^{W \times H}$  as the binary Fourier mask, parameterized by  $\sigma$ , that we used to filter high frequency, where each element  $\mathbf{K}^{\sigma}_{(i,j)}$  is determined as  $\mathbf{K}^{\sigma}_{(i,j)} = \mathbb{1}_{|i-\frac{W}{2}| \leq \sigma} \mathbb{1}_{|j-\frac{H}{2}| \leq \sigma}$ , with  $\mathbb{1}$  the indicator function and  $\bar{\mathbf{K}}^{\sigma} = 1 - \mathbf{K}^{\sigma}$ . As we have discussed above, the gradient of deep models is noisy, and in the following work, we consider that we only have access to  $\nabla_x \hat{f}(x)$ , a noisy estimator of  $\nabla_x f(x)$  such that  $\nabla_x \hat{f}(x) = \nabla_x f(x) + \varepsilon$  with  $\varepsilon \in \mathbb{R}^{W \times H}$ . We do not assume any randomness for the noise so far. The following proposition

develops the squared residual of the filtered noisy gradient as compared to the true one. Under the condition of finding the optimal filter, the gap between the two is naturally norm of the remaining noise post filtering.

**Proposition 3.1.** *Let  $\nabla \hat{\mathbf{f}} = \nabla \mathbf{f} + \varepsilon$  as the noisy gradient of  $\mathbf{f}$ , with  $\varepsilon \in \mathbb{R}^{W \times H}$ . For  $\sigma^* = \inf \{ \sigma : \|\mathcal{F}(\nabla \mathbf{f}) \odot \bar{\mathbf{K}}^\sigma\|_F^2 = 0 \}$ , we have*

$$\|\mathcal{F}^{-1}(\mathcal{F}(\nabla \hat{\mathbf{f}}) \odot \mathbf{K}^{\sigma^*}) - \nabla \mathbf{f}\|_F^2 = \|\mathcal{F}^{-1}(\mathcal{F}(\varepsilon) \odot \mathbf{K}^{\sigma^*})\|_F^2 \leq \|\varepsilon\|_F^2, \quad (1)$$

where  $\odot$  is the Hadamard product,  $\mathbf{K}^{\sigma^*}$  a binary mask for low-pass filtering of frequency  $\sigma$ , and  $\bar{\mathbf{K}}^{\sigma^*}$  is the opposite mask.

*Remark 3.2.* This result holds as long as we find  $\sigma^*$ . There always exists a  $\sigma^*$  as the set always contains  $\sigma = \max(H, W)$  which does not alter the Fourier spectrum of an image of size  $W \times H$ . However, finding  $\sigma^*$  poses a challenge, leading us to leverage XAI metrics as a heuristic.

With the information that the remaining gap between the filtered estimator and the true gradient is the remaining noise, of which the norm is upper bounded by the one of the original noise, we aim at measuring the reduction of the noise. In that way, we demonstrate the always-positive effect of **FORGrad** on gradient methods. In particular, under the assumption of Gaussian noise, we derive the distribution of the ratio  $\|\varepsilon\|_F^2 / \|\mathcal{F}^{-1}(\mathcal{F}(\varepsilon) \odot \mathbf{K}^{\sigma^*})\|_F^2$ .

**Proposition 3.3.** *Let the noise  $\varepsilon \in \mathbb{R}^{W \times H}$  follow a normal distribution  $\varepsilon \sim \mathcal{N}(0, \zeta)^{\otimes WH}$ . Then the norm of the Fourier spectra of the noise  $\|\mathcal{F}(\varepsilon)\|_F^2 \sim \Gamma(k = 2WH, \theta = \zeta^2 WH)$  and filtered noise  $\|\mathcal{F}(\varepsilon) \odot \mathbf{K}^\sigma\|_F^2 \sim \Gamma(k = 8\sigma^2, \theta = 4\zeta^2 \sigma^2)$  follows Gamma distributions.*

Therefore, the ratio of the two distributions  $R = \|\mathcal{F}(\varepsilon)\|_F^2 / \|\mathcal{F}(\varepsilon) \odot \mathbf{K}^\sigma\|_F^2$  follows a Beta prime distribution  $R \sim \beta'(2WH, 4\sigma^2, 1, \frac{WH}{4\sigma^2})$ .

This result allows us to directly compute the distribution of the ratio of the norm of the original noise on the norm of the filtered noise (up to a scaling factor, by Parseval's Theorem [55]). Naturally, this distribution depends on the parameter  $\sigma$  of the filtering. From this, we can deduce probabilistic results, such as, for  $\sigma = 10$  and  $\zeta = 1$ , the ratio of the norms is larger than 70 with probability almost one.

Finally, in the following proposition, we obtain a non-asymptotic result on the concentration of the SmoothGrad procedure to its expected value based on the Matrix Bernstein inequality [56].

**Proposition 3.4.** *We recall that SmoothGrad is defined as  $SG = \frac{1}{n} \sum_{i=1}^n \nabla_{\mathbf{x}} \mathbf{f}(\mathbf{x} + \delta_i)$  with  $\forall_{i=1, \dots, n} \delta_i \in \mathcal{N}(0, \zeta)^{\otimes WH}$ .  $\nabla_{\mathbf{x}} \mathbf{f}(\mathbf{x} + \delta_i)$  is a random matrix and therefore SG is. Assuming our predictor  $\mathbf{f} \in L\text{-Lip}(\mathcal{X})$  is  $L$ -Lipschitz. We denote  $\|\cdot\|_2$  as the spectral norm, and define the variance as  $\mathbb{V}(SG) = \max(\|\mathbb{E}((SG - \mathbb{E}SG) \cdot (SG - \mathbb{E}SG)^T)\|_2, \|\mathbb{E}((SG - \mathbb{E}SG)^T \cdot (SG - \mathbb{E}SG))\|_2)$ . We then have, for  $t > 0$ ,*

$$\mathbb{P}(\|SG - \mathbb{E}SG\|_2 \geq t) \leq (W + H) \cdot \exp\left(\frac{-t^2 n^2 / 2}{\mathbb{V}(SG) + 2Lt/3}\right). \quad (2)$$

Our results suggest that in order to effectively eliminate noise using the SmoothGrad method, several iterations are required as opposed to ours. For instance, to be at least  $t = \frac{L}{10}$  away from its expected value, with probability at most 0.01, we need  $n \approx 700$  iterations, for  $\zeta = 1$ . Furthermore, the noisy SmoothGrad gradually approaches the expected outcome of the non-noisy SmoothGrad. Additionally, SmoothGrad alleviates the noise but at the cost of employing Monte-Carlo sampling.

## 4 Gradient-based methods perform better and are more efficient

**The new explanations are free from noise** Figure 6 presents qualitative examples of corrected gradients obtained using the Gradient Input method [29] combined with **FORGrad**. As we analyze the different images, we observe that gradually removing high frequencies from the gradients has a notable impact on the resulting explanation. The initially noisy patterns transform into larger patches until the saliency map effectively highlights the key features that represent the object for categorization. However, it is crucial to consider the optimal value of  $\sigma^*$ , as exceeding this threshold leads to the map spreading too widely and the explanation becoming less informative. This observation is further supported by the curve on the right, which demonstrates the evolution of the faithfulness score as  $\sigma$  changes. Prior to finding the optimal  $\sigma$ , the faithfulness score fluctuates around the initial value before gradually increasing to reach its optimal level. As expected, when all the information is removed (represented by the last point on the x-axis), the fidelity score drops to zero.

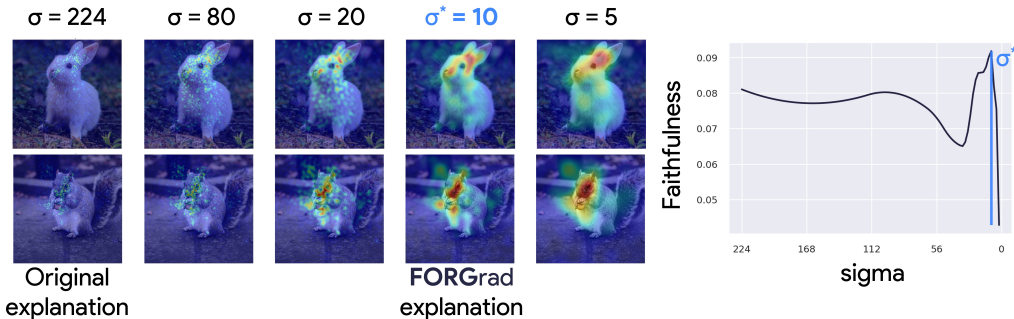


Figure 6: **FORGrad : selection of the optimal  $\sigma$** . With **FORGrad**, we aim to derive the explanation from the gradient’s corrected version. To achieve this, we determine the optimal cutoff of high frequencies in order to maximize the faithfulness of the explanation. The images displayed on the left illustrate the progression for different cutoff values. On the right side, the curve represents the variation of the metric across 1,000 images from the validation set of ImageNet, as a function of  $\sigma$ , representing the cutoff value.  $\sigma^*$  represents the optimal value, selected as the one maximizing the faithfulness score, equivalent to [Deletion-Insertion].

	ResNet50				ViT				ConvNeXT				
	Del.(↓)	Ins.(↑)	Fid.(↑)	Comp.	Del.(↓)	Ins.(↑)	Fid.(↑)	Comp.	Del.(↓)	Ins.(↑)	Fid.(↑)	Comp.	
Gradient-based	Saliency[4]	0.77	0.85	0.07	$\Theta(2)$	0.77	0.82	0.01	$\Theta(2)$	0.85	0.86	0.05	$\Theta(2)$
	Saliency*	0.74	0.90	0.15	$\Theta(2)$	0.81	0.89	0.03	$\Theta(2)$	0.82	0.88	0.06	$\Theta(2)$
	GradInput[29]	0.76	0.87	0.05	$\Theta(2)$	0.78	0.88	0.01	$\Theta(2)$	0.83	0.89	0.05	$\Theta(2)$
	GradInput*	0.74	0.88	0.13	$\Theta(2)$	<u>0.74</u>	0.89	<b>0.05</b>	$\Theta(2)$	<u>0.81</u>	0.88	<u>0.07</u>	$\Theta(2)$
	SmoothGrad[8]	0.74	0.89	0.08	$\Theta(200)$	0.80	0.87	0.03	$\Theta(200)$	0.86	0.86	0.05	$\Theta(200)$
	SmoothGrad*	<b>0.72</b>	<b>0.93</b>	<b>0.19</b>	$\Theta(200)$	0.78	<b>0.92</b>	<u>0.04</u>	$\Theta(200)$	0.82	0.88	0.06	$\Theta(200)$
	VarGrad[57]	0.74	0.91	0.07	$\Theta(200)$	<b>0.72</b>	0.88	0.01	$\Theta(200)$	0.89	0.86	0.02	$\Theta(200)$
	VarGrad*	<u>0.73</u>	0.91	<u>0.18</u>	$\Theta(200)$	0.74	0.90	0.02	$\Theta(200)$	<b>0.80</b>	0.88	0.02	$\Theta(200)$
	Int.Grad[9]	0.75	0.88	0.06	$\Theta(200)$	0.78	0.86	0.01	$\Theta(200)$	0.82	0.90	0.05	$\Theta(200)$
	Int.Grad*	0.74	0.89	0.15	$\Theta(200)$	0.79	0.87	0.03	$\Theta(200)$	<u>0.81</u>	0.90	0.05	$\Theta(200)$
Prediction-based	GradCAM[11]	0.78	<u>0.92</u>	0.06	$\Theta(2)$	n.a	n.a	n.a	n.a	0.87	0.92	0.06	$\Theta(2)$
	GradCAM++[58]	0.75	<b>0.93</b>	0.08	$\Theta(2)$	n.a	n.a	n.a	n.a	0.90	0.92	0.02	$\Theta(2)$
	Occlusion[29]	0.75	0.85	0.06	$\Theta(1024)$	0.79	0.83	0.01	$\Theta(1024)$	0.83	0.88	<u>0.07</u>	$\Theta(1024)$
	HSIC[16]	<b>0.72</b>	<u>0.92</u>	0.05	$\Theta(2000)$	0.77	<u>0.91</u>	0.02	$\Theta(2000)$	<b>0.80</b>	0.92	0.05	$\Theta(2000)$
	Sobel[59]	0.74	<u>0.92</u>	0.06	$\Theta(4000)$	0.79	<u>0.91</u>	0.02	$\Theta(4000)$	0.82	<u>0.93</u>	<b>0.08</b>	$\Theta(4000)$
	RISE[13]	0.76	<b>0.93</b>	0.07	$\Theta(8000)$	0.80	<b>0.92</b>	0.01	$\Theta(8000)$	0.84	<b>0.94</b>	<u>0.07</u>	$\Theta(8000)$

Table 1: **Results on Faithfulness metrics**. Deletion, Insertion, and Fidelity scores obtained on 1,000 ImageNet validation set images, on an Nvidia V100 (For Deletion, lower is better and for Insertion and Fidelity, higher is better). Complexity  $\Theta$  (Comp.) corresponds to the number of forward + backward passes required for computation, up to a factor that depends on the model. The first and second best results are in **bold** and underlined.

**A new ranking of attribution methods** We apply **FORGrad** on all the gradient-based attribution methods and report the scores in Table 1 for three models: ResNet50 [48], ViT [49] and ConvNeXT [50]. GradCAM methods can’t be tested on ViT because they are based on convolution so are limited to CNNs. We can observe two notable findings. Firstly, it is rare to encounter cases where the scores after applying **FORGrad** are lower than the scores obtained before. In such instances, the decrease in scores is typically observed in only one metric, either Deletion or Insertion. However, since the other metric is optimized, the overall Faithfulness, as measured by [Deletion-Insertion], remains at least as good as before. Secondly, even without explicitly optimizing the Fidelity metric, we observe an improvement in this score across all methods and the three models analyzed. Furthermore, after applying **FORGrad**, we observe that the scores of several gradient-based methods surpass or at least match those of prediction-based methods. Notably, these gradient-based methods offer the additional advantage of being significantly more computationally efficient, as evident from the complexity column. In order to determine the best method for each model, we propose to aggregate the scores from the three metrics to obtain a single global score for each method and model. This resulting score, is denoted as  $I(\varphi(x)) + F(\varphi(x)) - D(\varphi(x))$ , corresponding to the sum of 1-Deletion, Insertion and Fidelity score. Interestingly, in Table 2, we observe that the rankings change

	ResNet50		ViT		ConvNeXT	
	Original	<b>FORGrad</b>	Original	<b>FORGrad</b>	Original	<b>FORGrad</b>
1	GradCAM++	<b>SmoothGrad*</b>	VarGrad	<b>SmoothGrad*</b>	Sobol	Sobol
2	HSIC	<b>VarGrad*</b>	HSIC	<b>VarGrad*</b>	RISE	RISE
3	RISE	<b>Saliency*</b>	Sobol	HSIC	HSIC	HSIC
4	Sobol	<b>Int.Grad*</b>	RISE	Sobol	Occlusion	<b>GradInput*</b>
5	VarGrad	<b>GradInput*</b>	GradInput	RISE	GradCAM	<b>Int.Grad*</b>

Table 2: **Global ranking before (original) and after FORGrad.** For each model, we show the 5 attribution methods with highest metrics, before and after applying **FORGrad**. The explanation maps were computed on 1000 images from the validation set of ImageNet, based on an aggregation of the three metrics computed by  $I(\varphi(x)) + F(\varphi(x)) - D(\varphi(x))$ .

when we incorporate **FORGrad** into the analysis. This shift leads to the inclusion of at least two gradient-based methods among the top-5 for all three models. In the case of ResNet50, all five of the top-performing methods are gradient-based, whereas only one of them occupied a position in the previous ranking. Although some prediction-based methods, such as *Sobol* and *HSIC*, consistently demonstrate good performance, we demonstrate that gradient-based methods such as *SmoothGrad* and *VarGrad* now perform nearly as well, with the added advantage of computational efficiency.

## 5 Limitations

In our study, we have proposed to find an optimal  $\sigma$  value representing an ideal cutoff to improve explanations of gradient-based methods. However, we acknowledge that this optimal value is highly dependent on the dataset, perhaps more so than on the model itself. Furthermore, while we have chosen a single value that maximizes the scores across 1,000 images, it may be beneficial to use different values for individual images, but would increase the computational costs. We also optimize our value of  $\sigma$  only on 2 metrics, deletion and insertion. Even though it turns out to also increase the fidelity score, we could potentially obtain even better results by optimizing on this metric as well. It’s however, once again, a very resource-consuming method that we chose to avoid. Furthermore, in our ranking computation, we combine metrics that do not precisely capture the same information. While Deletion and Insertion can be aggregated, particularly since we optimize the difference between them, it should be noted that Deletion, Insertion, and Fidelity are not directly comparable even if they range between 0 and 1. We have proposed one approach to integrate these metrics and derive a ranking based on the three scores. However, an alternative could involve producing separate rankings for each individual score. If we had followed this approach, the **FORGrad** methods would have emerged as the top-5 for both ResNet50 and ViT, according to MuFidelity.

## 6 Conclusion

This work started with an empirical observation: prediction-based and gradient-based methods exhibit distinct power spectra in their attribution maps – with gradient-based methods exhibiting higher power in the high frequencies compared to prediction-based methods. This led us to wonder whether the frequency content of model gradients is merely noisy information. We demonstrate that removing this content does not impair our ability to approximate the gradient and conclude that high frequencies predominantly carry non-essential information. We further conducted an in-depth analysis of gradient frequency content in CNNs across processing layers and found that downsampling operations, such as max pooling and striding, contribute to the introduction of high frequencies. This points to model aliasing as a likely cause of this high-frequency content. Interestingly, even with training, CNNs are unable to prevent this phenomenon. These results hence raise the question: Could high-frequencies be filtered out to improve the explanations derived from attribution methods? We design an optimal filter,  $\sigma^*$ , and show that the filtering of attribution maps leads to significant improvements in the quality of the explanations. These improvements were most pronounced for gradient-based methods, which ended up approaching and sometimes even surpassing the much more compute-intensive prediction-based methods. Overall, our work leads to a surprising result – that the almost forgotten gradient-based methods turn out to contain all the information needed to provide a faithful explanation of a model’s decision and that they can be as interpretable as the newest methods. In future work, it would be worth exploring the influence of this noise on the model’s performance and evaluating whether replacing certain operations that introduce noise could affect both the accuracy and robustness of the models. Furthermore, considering that many adversarial attacks are gradient-based and often exploit additive noise patterns, it is worth investigating whether



these attacks target the noisy high-frequency content in the gradients and whether they might be prevented by using operations not introducing high-frequencies.

## 7 Acknowledgments

This work was supported to TS by ONR (N00014-19-1-2029), NSF (IIS-1912280 and EAR-1925481), DARPA (D19AC00015), NIH/NINDS (R21 NS 112743), the ANR-3IA Artificial and Natural Intelligence Toulouse Institute (ANR-19-PI3A-0004) to TS and RV. Additional support provided by the Carney Institute for Brain Science and the Center for Computation and Visualization (CCV). We acknowledge the Cloud TPU hardware resources that Google made available via the TensorFlow Research Cloud (TFRC) program as well as computing hardware supported by NIH Office of the Director grant S10OD025181.

## References

- [1] Alon Jacovi, Ana Marasović, Tim Miller, and Yoav Goldberg. Formalizing trust in artificial intelligence: Prerequisites, causes and goals of human trust in ai. In *Proceedings of the 2021 ACM conference on fairness, accountability, and transparency*, pages 624–635, 2021.
- [2] Finale Doshi-Velez and Been Kim. Towards a rigorous science of interpretable machine learning. *ArXiv e-print*, 2017.
- [3] Cynthia Rudin. Stop explaining black box machine learning models for high stakes decisions and use interpretable models instead. *Nature machine intelligence*, 1(5):206–215, 2019.
- [4] Karen Simonyan, Andrea Vedaldi, and Andrew Zisserman. Deep inside convolutional networks: Visualising image classification models and saliency maps. In *Workshop, Proceedings of the International Conference on Learning Representations (ICLR)*, 2013.
- [5] Karen Simonyan, Andrea Vedaldi, and Andrew Zisserman. Deep inside convolutional networks: Visualising image classification models and saliency maps. In *Workshop Proceedings of the International Conference on Learning Representations (ICLR)*, 2014.
- [6] Matthew D Zeiler and Rob Fergus. Visualizing and understanding convolutional networks. In *Proceedings of the IEEE European Conference on Computer Vision (ECCV)*, 2014.
- [7] Jost Tobias Springenberg, Alexey Dosovitskiy, Thomas Brox, and Martin Riedmiller. Striving for simplicity: The all convolutional net. In *Workshop Proceedings of the International Conference on Learning Representations (ICLR)*, 2014.
- [8] Daniel Smilkov, Nikhil Thorat, Been Kim, Fernanda Viégas, and Martin Wattenberg. Smoothgrad: removing noise by adding noise. In *Workshop on Visualization for Deep Learning, Proceedings of the International Conference on Machine Learning (ICML)*, 2017.
- [9] Mukund Sundararajan, Ankur Taly, and Qiqi Yan. Axiomatic attribution for deep networks. In *Proceedings of the International Conference on Machine Learning (ICML)*, 2017.
- [10] Bolei Zhou, Aditya Khosla, Agata Lapedriza, Aude Oliva, and Antonio Torralba. Learning deep features for discriminative localization. In *Proceedings of the IEEE conference on computer vision and pattern recognition*, pages 2921–2929, 2016.
- [11] Ramprasaath R. Selvaraju, Michael Cogswell, Abhishek Das, Ramakrishna Vedantam, Devi Parikh, and Dhruv Batra. Grad-cam: Visual explanations from deep networks via gradient-based localization. In *Proceedings of the IEEE International Conference on Computer Vision (ICCV)*, 2017.
- [12] Ruth C. Fong and Andrea Vedaldi. Interpretable explanations of black boxes by meaningful perturbation. In *Proceedings of the IEEE International Conference on Computer Vision (ICCV)*, 2017.
- [13] Vitali Petsiuk, Abir Das, and Kate Saenko. Rise: Randomized input sampling for explanation of black-box models. In *Proceedings of the British Machine Vision Conference (BMVC)*, 2018.
- [14] Thomas Fel, Rémi Cadène, Mathieu Chalvidal, Matthieu Cord, David Vigouroux, and Thomas Serre. Look at the variance! efficient black-box explanations with sobol-based sensitivity analysis. *Advances in Neural Information Processing Systems*, 34:26005–26014, 2021.
- [15] Marco Tulio Ribeiro, Sameer Singh, and Carlos Guestrin. "why should i trust you?": Explaining the predictions of any classifier. In *Knowledge Discovery and Data Mining (KDD)*, 2016.
- [16] Paul Novello, Thomas Fel, and David Vigouroux. Making sense of dependence: Efficient black-box explanations using dependence measure. In *Advances in Neural Information Processing Systems (NeurIPS)*, 2022.



- [17] Leon Sixt, Maximilian Granz, and Tim Landgraf. When explanations lie: Why many modified by attributions fail. In *Proceedings of the International Conference on Machine Learning (ICML)*, 2020.
- [18] Julius Adebayo, Justin Gilmer, Michael Muellly, Ian Goodfellow, Moritz Hardt, and Been Kim. Sanity checks for saliency maps. In *Advances in Neural Information Processing Systems (NIPS)*, 2018.
- [19] Dylan Slack, Anna Hilgard, Sameer Singh, and Himabindu Lakkaraju. Reliable post hoc explanations: Modeling uncertainty in explainability. *Advances in Neural Information Processing Systems (NeurIPS)*, 34, 2021.
- [20] Tessa Han, Suraj Srinivas, and Himabindu Lakkaraju. Which explanation should i choose? a function approximation perspective to characterizing post hoc explanations. In *Advances in Neural Information Processing Systems (NeurIPS)*, 2022.
- [21] Chirag Agarwal, Nari Johnson, Martin Pawelczyk, Satyapriya Krishna, Eshika Saxena, Marinka Zitnik, and Himabindu Lakkaraju. Rethinking stability for attribution-based explanations. In *ICLR 2022 Workshop on PAIR 2Struct: Privacy, Accountability, Interpretability, Robustness, Reasoning on Structured Data*.
- [22] Sushant Agarwal, Shahin Jabbari, Chirag Agarwal, Sohini Upadhyay, Steven Wu, and Himabindu Lakkaraju. Towards the unification and robustness of perturbation and gradient based explanations. In *Proceedings of the International Conference on Machine Learning (ICML)*, 2021.
- [23] Rattana Pukdee, Dylan Sam, J Zico Kolter, Maria-Florina Balcan, and Pradeep Ravikumar. Learning with explanation constraints. *arXiv preprint arXiv:2303.14496*, 2023.
- [24] Beomsu Kim, Junghoon Seo, Seunghyeon Jeon, Jamyoungh Koo, Jeongyeol Choe, and Taegyun Jeon. Why are saliency maps noisy? cause of and solution to noisy saliency maps. In *2019 IEEE/CVF International Conference on Computer Vision Workshop (ICCVW)*, pages 4149–4157. IEEE, 2019.
- [25] Ramprasaath R Selvaraju, Michael Cogswell, Abhishek Das, Ramakrishna Vedantam, Devi Parikh, and Dhruv Batra. Grad-cam: Visual explanations from deep networks via gradient-based localization. In *Proceedings of the IEEE international conference on computer vision*, pages 618–626, 2017.
- [26] Sukrut Rao, Moritz Böhle, and Bernt Schiele. Towards better understanding attribution methods. In *Proceedings of the IEEE Conference on Computer Vision and Pattern Recognition (CVPR)*, 2022.
- [27] Richard Tomsett, Dan Harborne, Supriyo Chakraborty, Prudhvi Gurrum, and Alun Preece. Sanity checks for saliency metrics. In *Proceedings of the AAAI Conference on Artificial Intelligence (AAAI)*, 2019.
- [28] Amirata Ghorbani, Abubakar Abid, and James Zou. Interpretation of neural networks is fragile. In *Proceedings of the AAAI Conference on Artificial Intelligence (AAAI)*, 2017.
- [29] Marco Ancona, Enea Ceolini, Cengiz Öztireli, and Markus Gross. Towards better understanding of gradient-based attribution methods for deep neural networks. In *Proceedings of the International Conference on Learning Representations (ICLR)*, 2018.
- [30] Giang Nguyen, Daeyoung Kim, and Anh Nguyen. The effectiveness of feature attribution methods and its correlation with automatic evaluation scores. *Advances in Neural Information Processing Systems (NeurIPS)*, 2021.
- [31] Sunnie S. Y. Kim, Nicole Meister, Vikram V. Ramaswamy, Ruth Fong, and Olga Russakovsky. HIVE: Evaluating the human interpretability of visual explanations. In *Proceedings of the IEEE European Conference on Computer Vision (ECCV)*, 2022.
- [32] Julien Colin, Thomas Fel, Rémi Cadène, and Thomas Serre. What i cannot predict, i do not understand: A human-centered evaluation framework for explainability methods. *Advances in Neural Information Processing Systems (NeurIPS)*, 2021.
- [33] Mathieu Serrurier, Franck Mamalet, Thomas Fel, Louis Béthune, and Thibaut Boissin. When adversarial attacks become interpretable counterfactual explanations. *arXiv preprint arXiv:2206.06854*, 2022.
- [34] Peter Hase and Mohit Bansal. Evaluating explainable ai: Which algorithmic explanations help users predict model behavior? *Proceedings of the Annual Meeting of the Association for Computational Linguistics (ACL)*, 2020.
- [35] Marouane El Idrissi, Nicolas Bousquet, Fabrice Gamboa, Bertrand Iooss, and Jean-Michel Loubes. On the coalitional decomposition of parameters of interest, 2023.
- [36] David Baehrens, Timon Schroeter, Stefan Harmeling, Motoaki Kawanabe, Katja Hansen, and Klaus-Robert Müller. How to explain individual classification decisions. *The Journal of Machine Learning Research*, 11: 1803–1831, 2010.
- [37] Zhiqin John Xu. Understanding training and generalization in deep learning by fourier analysis. *arXiv preprint arXiv:1808.04295*, 2018.
- [38] Dong Yin, Raphael Gontijo Lopes, Jon Shlens, Ekin Dogus Cubuk, and Justin Gilmer. A fourier perspective on model robustness in computer vision. *Advances in Neural Information Processing Systems*, 32, 2019.

- [39] Yusuke Tsuzuku and Issei Sato. On the structural sensitivity of deep convolutional networks to the directions of fourier basis functions. In *Proceedings of the IEEE/CVF Conference on Computer Vision and Pattern Recognition*, pages 51–60, 2019.
- [40] Gintare Karolina Dziugaite, Zoubin Ghahramani, and Daniel M Roy. A study of the effect of jpg compression on adversarial images. *arXiv preprint arXiv:1608.00853*, 2016.
- [41] Chuan Guo, Mayank Rana, Moustapha Cisse, and Laurens Van Der Maaten. Countering adversarial images using input transformations. *arXiv preprint arXiv:1711.00117*, 2017.
- [42] Sibong Song, Yueru Chen, Ngai-Man Cheung, and C-C Jay Kuo. Defense against adversarial attacks with saak transform. *arXiv preprint arXiv:1808.01785*, 2018.
- [43] Jason Jo and Yoshua Bengio. Measuring the tendency of cnns to learn surface statistical regularities. *arXiv preprint arXiv:1711.11561*, 2017.
- [44] Ramesh C. Jain, Rangachar Kasturi, and Brian G. Schunck. *Machine vision*. 1995.
- [45] Said Pertuz, Domenec Puig, and Miguel Angel Garcia. Analysis of focus measure operators for shape-from-focus. *Pattern Recognition*, 46(5):1415–1432, 2013.
- [46] Hector Zenil, Jean-Paul Delahaye, and Cédric Gaucherel. Image characterization and classification by physical complexity. *Complexity*, 17(3):26–42, 2012.
- [47] Andrei N Kolmogorov. On tables of random numbers. *Sankhyā: The Indian Journal of Statistics, Series A*, pages 369–376, 1963.
- [48] Kaiming He, Xiangyu Zhang, Shaoqing Ren, and Jian Sun. Deep residual learning for image recognition. In *Proceedings of the IEEE Conference on Computer Vision and Pattern Recognition (CVPR)*, 2016.
- [49] Alexey Dosovitskiy, Lucas Beyer, Alexander Kolesnikov, Dirk Weissenborn, Xiaohua Zhai, Thomas Unterthiner, Mostafa Dehghani, Matthias Minderer, Georg Heigold, Sylvain Gelly, et al. An image is worth 16x16 words: Transformers for image recognition at scale. *arXiv preprint arXiv:2010.11929*, 2020.
- [50] Zhuang Liu, Hanzi Mao, Chao-Yuan Wu, Christoph Feichtenhofer, Trevor Darrell, and Saining Xie. A convnet for the 2020s. In *Proceedings of the IEEE/CVF Conference on Computer Vision and Pattern Recognition (CVPR)*, pages 11976–11986, June 2022.
- [51] Chris Olah, Alexander Mordvintsev, and Ludwig Schubert. Feature visualization. *Distill*, 2017. doi: 10.23915/distill.00007. <https://distill.pub/2017/feature-visualization>.
- [52] Xueyan Zou, Fanyi Xiao, Zhiding Yu, Yuheng Li, and Yong Jae Lee. Delving deeper into anti-aliasing in convnets. *International Journal of Computer Vision*, 131(1):67–81, 2023.
- [53] Karen Simonyan and Andrew Zisserman. Very deep convolutional networks for large-scale image recognition. *arXiv preprint arXiv:1409.1556*, 2014.
- [54] Umang Bhatt, Adrian Weller, and José MF Moura. Evaluating and aggregating feature-based model explanations. *arXiv preprint arXiv:2005.00631*, 2020.
- [55] Marc-Antoine Parseval. Mémoire sur les séries et sur l’intégration complète d’une équation aux différences partielles linéaires du second ordre, à coefficients constants. *Mém. prés. par divers savants, Acad. des Sciences, Paris*, (1), 1:638–648, 1806.
- [56] Joel A Tropp et al. An introduction to matrix concentration inequalities. *Foundations and Trends® in Machine Learning*, 8(1-2):1–230, 2015.
- [57] Junghoon Seo, Jeongyeol Choe, Jamiyoung Koo, Seunghyeon Jeon, Beomsu Kim, and Taegyun Jeon. Noise-adding methods of saliency map as series of higher order partial derivative. In *Workshop on Human Interpretability in Machine Learning, Proceedings of the International Conference on Machine Learning (ICML)*, 2018.
- [58] Aditya Chattopadhyay, Anirban Sarkar, Prantik Howlader, and Vineeth N Balasubramanian. Grad-cam++: Generalized gradient-based visual explanations for deep convolutional networks. In *Proceedings of the IEEE/CVF Winter Conference on Applications of Computer Vision (WACV)*, 2018.
- [59] Thomas Fel, Remi Cadene, Mathieu Chalvidal, Matthieu Cord, David Vigouroux, and Thomas Serre. Look at the variance! efficient black-box explanations with sobol-based sensitivity analysis. In *Advances in Neural Information Processing Systems (NeurIPS)*, 2021.

## A Proofs

In this section, we build on the assumption – that we empirically showed in the paper – that the gradient is noisy and demonstrate, through a Fourier perspective, that **FORGrad** method effectively recovers the true gradient. We then propose a convergence bound for SmoothGrad, showing that it

also recovers the true gradient at the cost of multiple samplings, and provide convergence bounds as well.

As a recall, we still consider a predictor  $\mathbf{f}(\cdot)$  that maps datum from an input space  $\mathcal{X} \subseteq \mathbb{R}^{W \times H}$  (with  $W, H$  being positive integers) to an output space  $\mathcal{Y} \subseteq \mathbb{R}$ . Moreover,  $\mathcal{F}$  and  $\mathcal{F}^{-1}$  still denote the Discrete Fourier Transform (DFT) on  $\mathcal{X}$  and its inverse. We assume that  $\mathbf{f}$  is  $L$ -lipschitz. We recall that a function  $\mathbf{f}$  is said  $L$ -lipschitz  $\mathbf{f} \in Lip(\mathcal{X})$  if and only if  $\forall (\mathbf{x}, \mathbf{z}) \in \mathcal{X}^2, \|\mathbf{f}(\mathbf{x}) - \mathbf{f}(\mathbf{z})\| \leq L\|\mathbf{x} - \mathbf{z}\|$ , with  $L \in \mathbb{R}$ . Finally, we define  $\mathbf{K}^\sigma \in \{0, 1\}^{W \times H}$  as the binary mask parametrized by  $\sigma$  that we used to filter high frequency, where each element  $\mathbf{K}_{(i,j)}^\sigma$  is determined as follows:

$$\mathbf{K}_{(i,j)}^\sigma = \begin{cases} 1, & \text{if } |i - \frac{W}{2}| \leq \sigma \text{ and } |j - \frac{H}{2}| \leq \sigma, \\ 0, & \text{otherwise.} \end{cases}$$

**Definition A.1.** Noisy gradient. Let  $\mathbf{f}$  be differentiable and  $\nabla_{\mathbf{x}}\mathbf{f}(\mathbf{x})$  denote the gradient of  $\mathbf{f}$  in  $\mathbf{x}$ . We consider that we only have access to  $\nabla_{\mathbf{x}}\hat{\mathbf{f}}(\mathbf{x})$ , a noisy estimator of  $\nabla_{\mathbf{x}}\mathbf{f}(\mathbf{x})$  such that  $\nabla_{\mathbf{x}}\hat{\mathbf{f}}(\mathbf{x}) = \nabla_{\mathbf{x}}\mathbf{f}(\mathbf{x}) + \varepsilon$  with  $\varepsilon \in \mathbb{R}^{W \times H}$ . We denote  $\|\cdot\|_F$  as the Frobenius norm.

So far, we do not consider this noise to be random, and we aim at bounding the leftover noise after the application of our method. In particular, we'll notice that at the level  $\sigma^*$ , it only depends on the value of  $\sigma^*$  and is always upper bounded by the norm of the original noise.

**Proposition A.2.** Let  $\nabla\hat{\mathbf{f}} = \nabla\mathbf{f} + \varepsilon$  as the noisy gradient of  $\mathbf{f}$ , with  $\varepsilon \in \mathbb{R}^{W \times H}$ . For  $\sigma^* = \inf \{\sigma : \|\mathcal{F}(\nabla\mathbf{f}) \odot \bar{\mathbf{K}}^\sigma\|_F^2 = 0\}$ , we have

$$\|\mathcal{F}^{-1}(\mathcal{F}(\nabla\hat{\mathbf{f}}) \odot \mathbf{K}^{\sigma^*}) - \nabla\mathbf{f}\|_F^2 = \|\mathcal{F}^{-1}(\mathcal{F}(\varepsilon) \odot \mathbf{K}^{\sigma^*})\|_F^2 \leq \|\varepsilon\|_F^2, \quad (3)$$

where  $\odot$  is the Hadamard product,  $\mathbf{K}^{\sigma^*}$  a binary mask for low-pass filtering of frequency  $\sigma$ , and  $\bar{\mathbf{K}}^{\sigma^*}$  is the opposite mask.

*Proof.*

$$\|\mathcal{F}^{-1}(\mathcal{F}(\nabla\hat{\mathbf{f}} \odot \mathbf{K}^\sigma)) - \nabla\mathbf{f}\|_F^2 = \|\mathcal{F}^{-1}(\mathcal{F}(\nabla\hat{\mathbf{f}} \odot \mathbf{K}^\sigma)) - \mathcal{F}^{-1}(\mathcal{F}(\nabla\mathbf{f}))\|_F^2 \quad (4)$$

$$= \|\mathcal{F}^{-1}(\mathcal{F}(\nabla\mathbf{f} + \varepsilon \odot \mathbf{K}^\sigma)) - \mathcal{F}^{-1}(\mathcal{F}(\nabla\mathbf{f}))\|_F^2 \quad (5)$$

$$= \|\mathcal{F}^{-1}(\mathcal{F}(\nabla\mathbf{f} \odot \mathbf{K}^\sigma) + \mathcal{F}(\varepsilon \odot \mathbf{K}^\sigma)) - \mathcal{F}^{-1}(\mathcal{F}(\nabla\mathbf{f}))\|_F^2 \quad (6)$$

$$= \|\mathcal{F}^{-1}(\mathcal{F}(\nabla\mathbf{f} \odot \mathbf{K}^\sigma) + \mathcal{F}(\varepsilon \odot \mathbf{K}^\sigma) - \mathcal{F}(\nabla\mathbf{f}))\|_F^2 \quad (7)$$

$$= \|\mathcal{F}^{-1}(\mathcal{F}(\varepsilon \odot \mathbf{K}^\sigma) - \mathcal{F}(\nabla\mathbf{f} \odot \bar{\mathbf{K}}^\sigma))\|_F^2 \quad (8)$$

$$(9)$$

Then by selecting  $\sigma^* = \in \mathbf{f} \{\sigma : \|\mathcal{F}(\nabla\mathbf{f} \odot \bar{\mathbf{K}}^\sigma) - \mathcal{F}(\nabla\mathbf{f})\|_F^2 = 0\}$ , we have that

$$\|\mathcal{F}^{-1}(\mathcal{F}(\varepsilon \odot \mathbf{K}^\sigma) - \mathcal{F}(\nabla\mathbf{f} \odot \bar{\mathbf{K}}^\sigma))\|_F^2 = \|\mathcal{F}^{-1}(\mathcal{F}(\varepsilon) \odot \mathbf{K}^\sigma)\|_F^2 \quad (10)$$

$$\leq \|\varepsilon\|_F^2 \quad (11)$$

$$(12)$$

□

Now, by adding an assumption of randomness on the noise  $\varepsilon$ , we can deduce the distribution of the ratio of the two last members of the previous proposition, and deduce an order of scale of the norm of the remaining noise after filtration, compared to its original norm.

**Proposition A.3.** Let the noise  $\varepsilon \in \mathbb{R}^{W \times H}$  follow a normal distribution  $\varepsilon \sim \mathcal{N}(0, \varsigma)^{\otimes WH}$ . Then the norm of the Fourier spectra of the noise  $\|\mathcal{F}(\varepsilon)\|_F^2 \sim \Gamma(k = 2WH, \theta = \varsigma^2WH)$  and filtered noise  $\|\mathcal{F}(\varepsilon) \odot \mathbf{K}^\sigma\|_F^2 \sim \Gamma(k = 8\sigma^2, \theta = 4\varsigma^2\sigma^2)$  follows Gamma distributions.

Therefore, the ratio of the two distributions  $R = \|\mathcal{F}(\varepsilon)\|_F^2 / \|\mathcal{F}(\varepsilon) \odot \mathbf{K}^\sigma\|_F^2$  follows a Beta prime distribution  $R \sim \beta'(2WH, 4\sigma^2, 1, \frac{WH}{4\sigma^2})$ .

*Proof.* As defined previously,  $\varepsilon_{(i,j)} \sim \mathcal{N}(0, \varsigma)$ . It is well known that the Fourier transform of that random matrix follows a complex normal distribution, or equivalently the real and imaginary random variables of the Fourier transform are i.i.d normally distributed, as  $\mathcal{RF}(\varepsilon)_{(i,j)} \sim \mathcal{N}(0, \varsigma\sqrt{WH/2})$  and  $\mathcal{IF}(\varepsilon)_{(i,j)} \sim \mathcal{N}(0, \varsigma\sqrt{WH/2})$ . Therefore the scaled norm follows a  $\chi^2$  distribution.

$$\frac{\|\mathcal{F}(\varepsilon)\|_F^2}{\varsigma\sqrt{WH/2}} \sim \chi_{2WH}^2 \quad \text{and equivalently,} \quad \frac{\|\mathcal{F}(\varepsilon) \odot \mathbf{K}^\sigma\|_F^2}{\varsigma\sqrt{WH/2}} \sim \chi_{8\sigma^2}^2. \quad (13)$$

Note that  $\chi^2$  distributions are a specific case of Gamma distributions, and can therefore be noted as follows  $\|\mathcal{F}(\varepsilon)\|_F^2 \sim \Gamma(k = WH, \theta = \varsigma^2WH)$  and filtered noise  $\|\mathcal{F}(\varepsilon) \odot \mathbf{K}^\sigma\|_F^2 \sim \Gamma(k = 4\sigma^2, \theta = 4\varsigma^2\sigma^2)$ . Finally, let  $R = \|\mathcal{F}(\varepsilon)\|_F^2 / \|\mathcal{F}(\varepsilon) \odot \mathbf{K}^\sigma\|_F^2$ . Since both random variables follow a Gamma distribution, their ratio is a Beta prime distribution of parameters  $R \sim \beta'(WH, 4\sigma^2, 1, \frac{WH}{4\sigma^2})$ .

The results remain valid in the input space by Parseval's Theorem [55], up to a constant factor.  $\square$

**Proposition A.4.** *We recall that SmoothGrad is defined as  $SG = \frac{1}{n} \sum_{i=1}^n \nabla_{\mathbf{x}} \mathbf{f}(\mathbf{x} + \delta_i)$  with  $\forall_{i=1, \dots, n} \delta_i \in \mathcal{N}(0, \varsigma)^{\otimes WH}$ .  $\nabla_{\mathbf{x}} \mathbf{f}(\mathbf{x} + \delta_i)$  is a random matrix and therefore SG is. Assuming our predictor  $\mathbf{f} \in L\text{-Lip}(\mathcal{X})$  is  $L$ -Lipschitz. We denote  $\|\cdot\|_2$  as the spectral norm, and define the variance as  $\mathbb{V}(SG) = \max(\|\mathbb{E}((SG - \mathbb{E}SG) \cdot (SG - \mathbb{E}SG)^T)\|_2, \|\mathbb{E}((SG - \mathbb{E}SG)^T \cdot (SG - \mathbb{E}SG))\|_2)$ . We then have, for  $t > 0$ ,*

$$\mathbb{P}(\|SG - \mathbb{E}SG\|_2 \geq t) \leq (W + H) \cdot \exp\left(\frac{-t^2 n^2 / 2}{\mathbb{V}(SG) + 2Lt/3}\right). \quad (14)$$

*Proof.* We first demonstrate the bounded difference property

$$\forall_{i=1, \dots, n} \|\nabla_{\mathbf{x}} \mathbf{f}(\mathbf{x} + \delta_i) - \mathbb{E} \nabla_{\mathbf{x}} \mathbf{f}(\mathbf{x} + \delta_i)\|_2 \leq \|\nabla_{\mathbf{x}} \mathbf{f}(\mathbf{x} + \delta_i)\|_2 + \|\mathbb{E} \nabla_{\mathbf{x}} \mathbf{f}(\mathbf{x} + \delta_i)\|_2 \leq 2L. \quad (15)$$

Finally, the result follows by application of the Matrix Bernstein Inequality [56].  $\square$

## B Different measures of complexity

To corroborate the results in S3.1 and S3.3 computing the high-frequency content from Kolmogorov image compression metric, we reproduce those experiments using the Laplace2-operator. We additionally show the evolution of high-frequency content in VGG16 and ViT using both metrics. On all the plots, we observe a similar trend between the metrics, confirming that :

- Gradient-based and prediction-based methods have a different signature in the Fourier spectrum (see Figure 7)
- On both convolutional models (ResNet50 and VGG) we observe more high frequencies when the models contain an MaxPooling operation or strided convolution instead of AveragePooling (see Figures 8, 9, 9, top curves)
- On both convolutional models, training the model doesn't alleviate the high frequency content (see Figures 8, 9, 9, bottom curves). However, we observe a different behaviour on ViT, suggesting that a different mechanism is responsible for the high-frequency content in this kind of architectures (see Figures 11, 12).

### B.1 For the methods

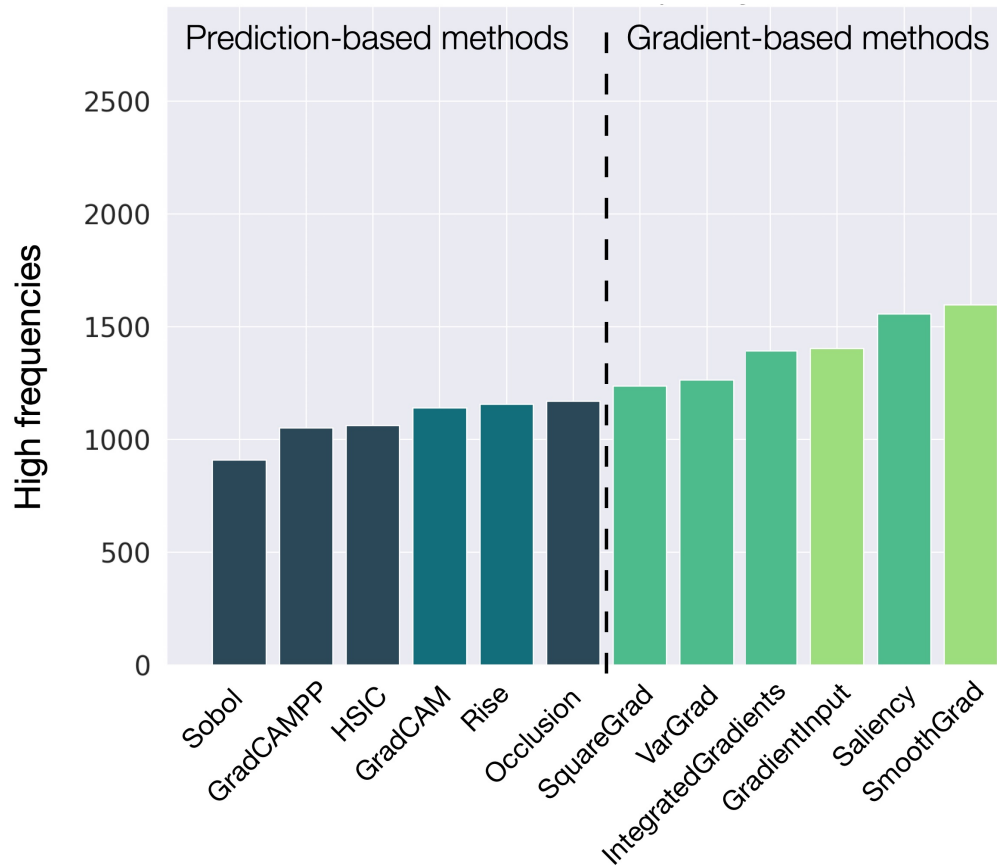


Figure 7: **High-frequency power in attribution methods.** High-frequency power present in the importance maps derived from different attribution methods, computed using Laplacian2 operator. Prediction-based methods produce less high-frequency content than gradient-based methods.

## B.2 For the models

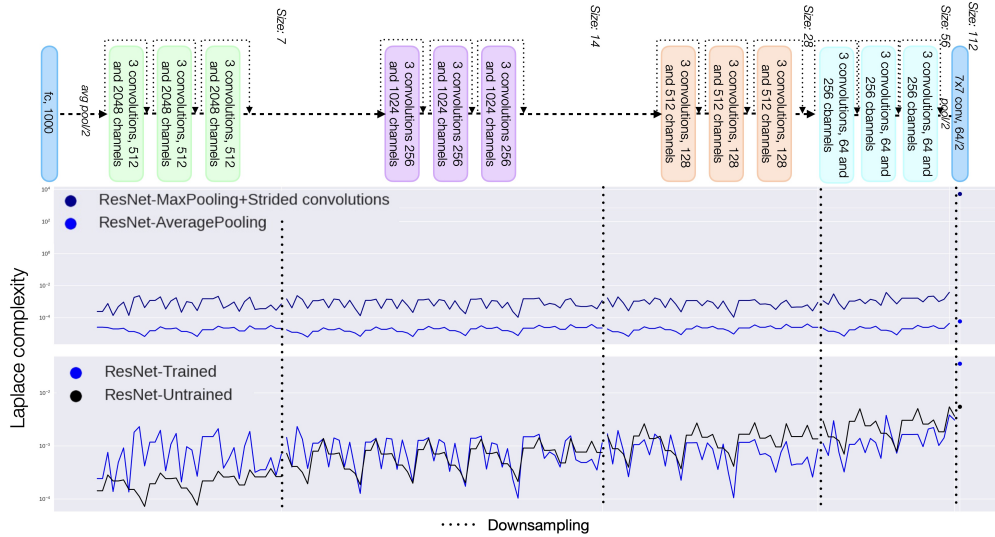


Figure 8: **Evolution of the high-frequency content in Resnet50.** We compute the high-frequency content along the depth of a ResNet50 varying either the weights or the pooling, using Laplace2-operator. The top curve illustrates the impact of different poolings, with MaxPooling and stride shown in dark blue and AveragePooling in light blue. The bottom curve represents the trained model, indicated by the blue curve, while the untrained model is represented by the black curve. Each point on the graph corresponds to a layer within the model.



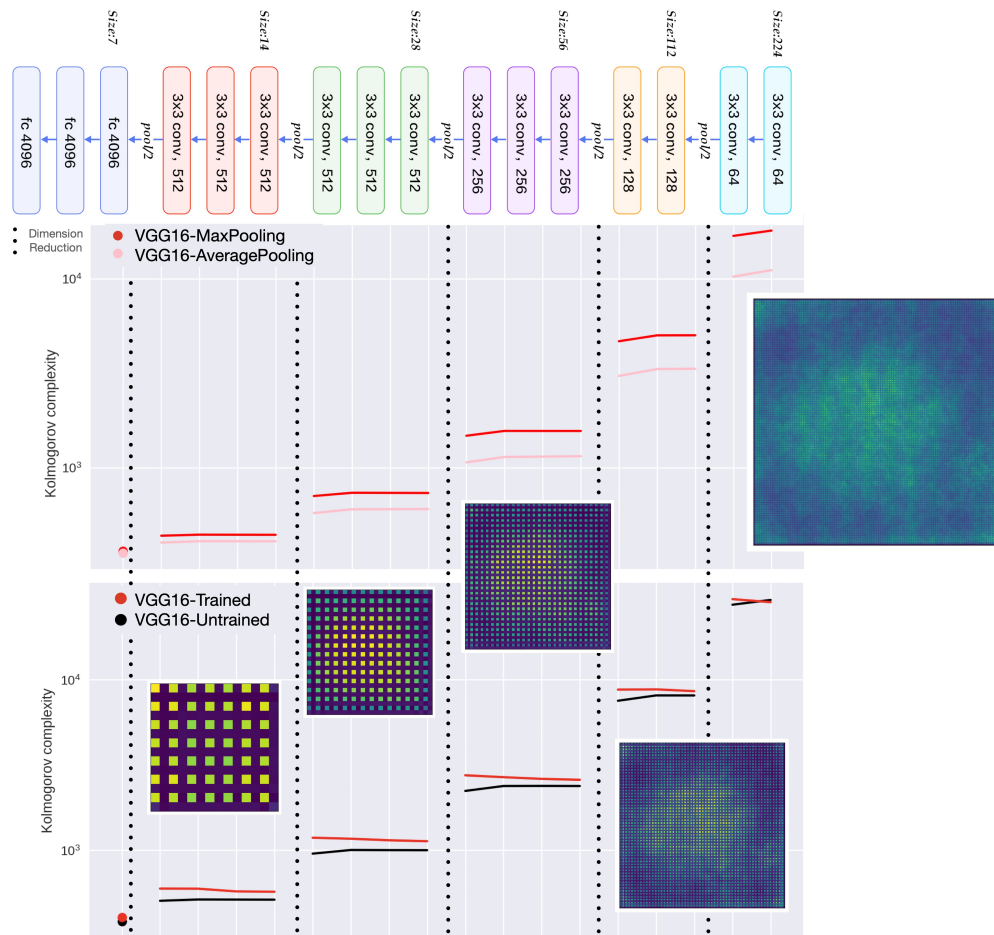


Figure 9: **Evolution of the high-frequency content in VGG16 with Kolmogorov complexity.** We compute the high-frequency content along the depth of a VGG16 varying either the weights or the pooling, using Kolmogorov image compression. The top curve illustrates the impact of different poolings, with MaxPooling shown in dark red and AveragePooling in pink. The bottom curve represents the trained model, indicated by the red curve, while the untrained model is represented by the black curve. Each point on the graph corresponds to a layer within the model.

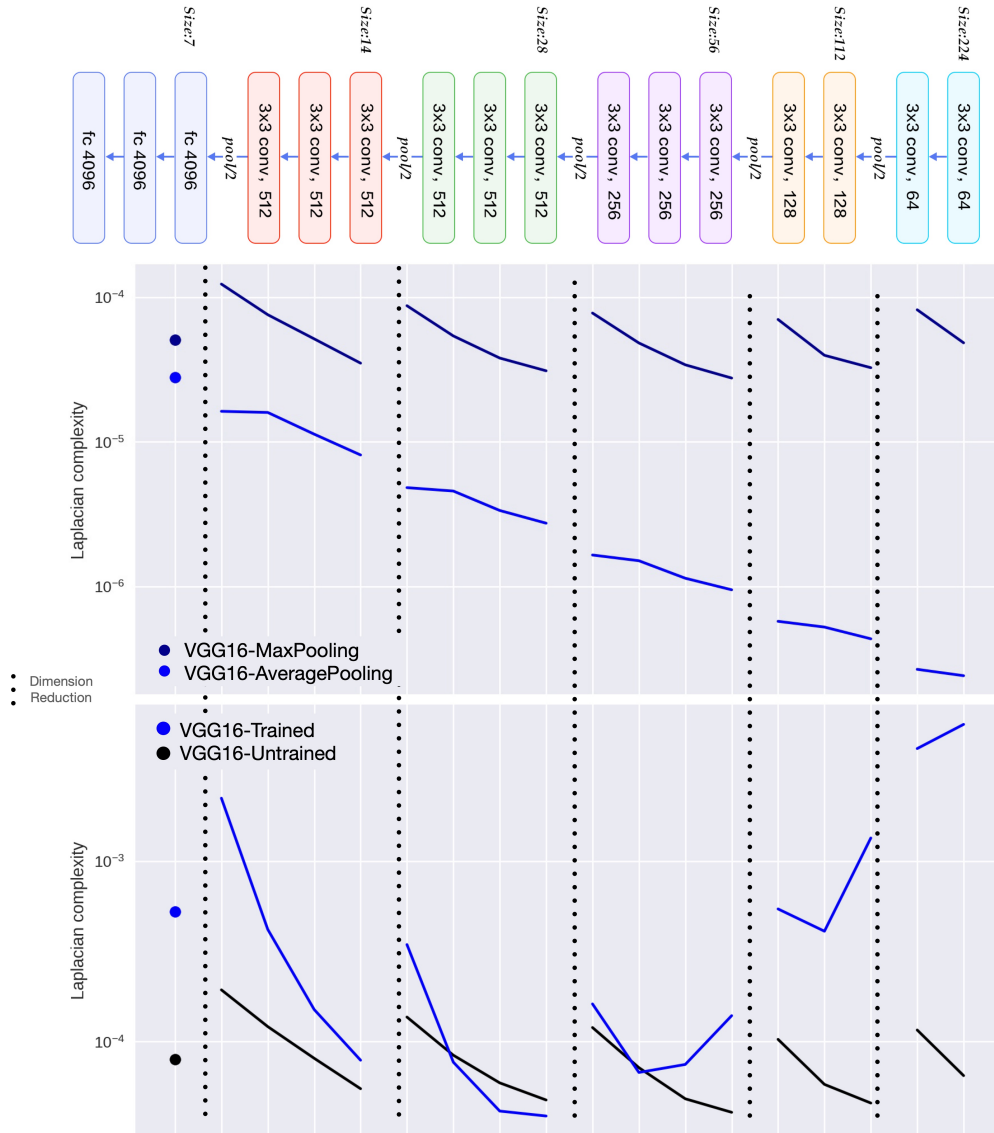


Figure 10: **Evolution of the high-frequency content in VGG16 with Laplace complexity.** We compute the high-frequency content along the depth of a VGG16 varying either the weights or the pooling, using Laplace2-operator. The top curve illustrates the impact of different poolings, with MaxPooling shown in dark blue and AveragePooling in light blue. The bottom curve represents the trained model, indicated by the blue curve, while the untrained model is represented by the black curve. Each point on the graph corresponds to a layer within the model.

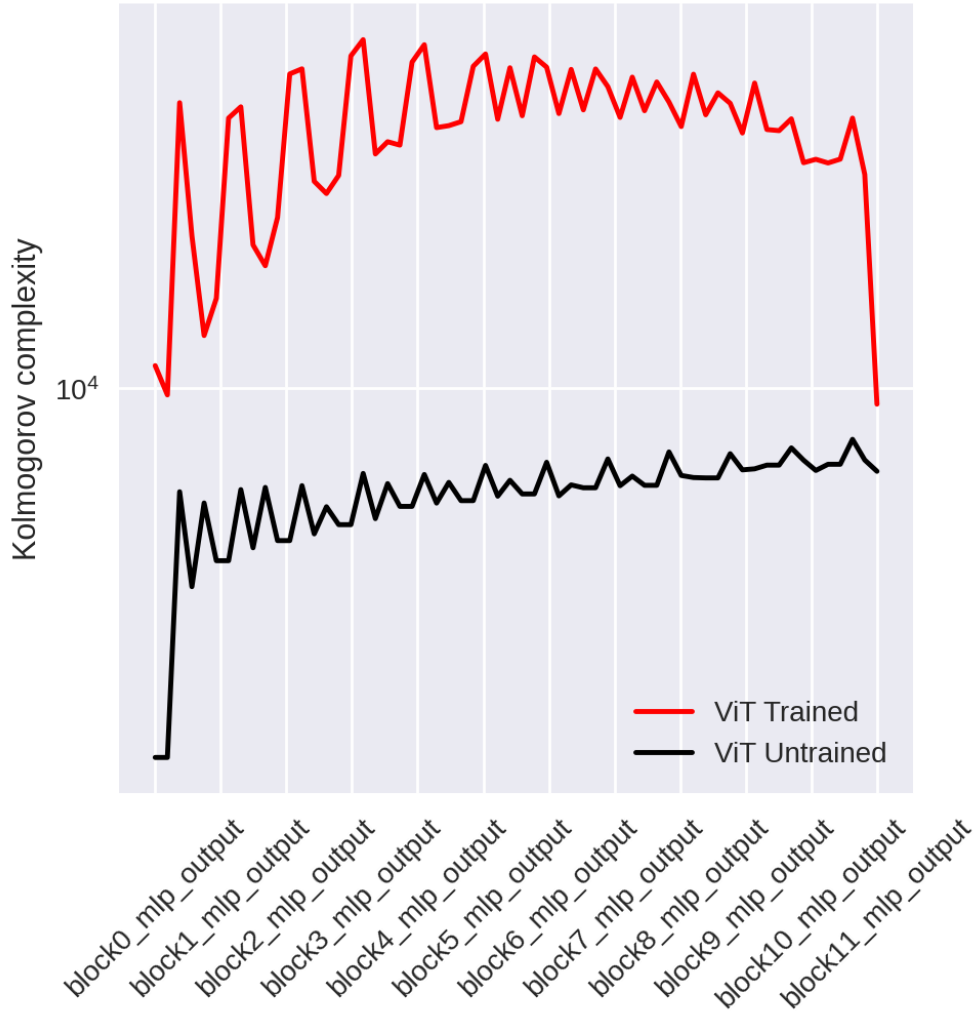


Figure 11: **Evolution of the high-frequency content in ViT with Kolmogorov complexity.** We compute the high-frequency content along the depth of a ViT varying the weights, using Kolmogorov image compression. The curve represents the trained model, indicated by the red curve, while the untrained model is represented by the black curve. Each point on the graph corresponds to a layer within the model. We show the labels representing the end of a block to give an idea of the evolution of the complexity inside a block.

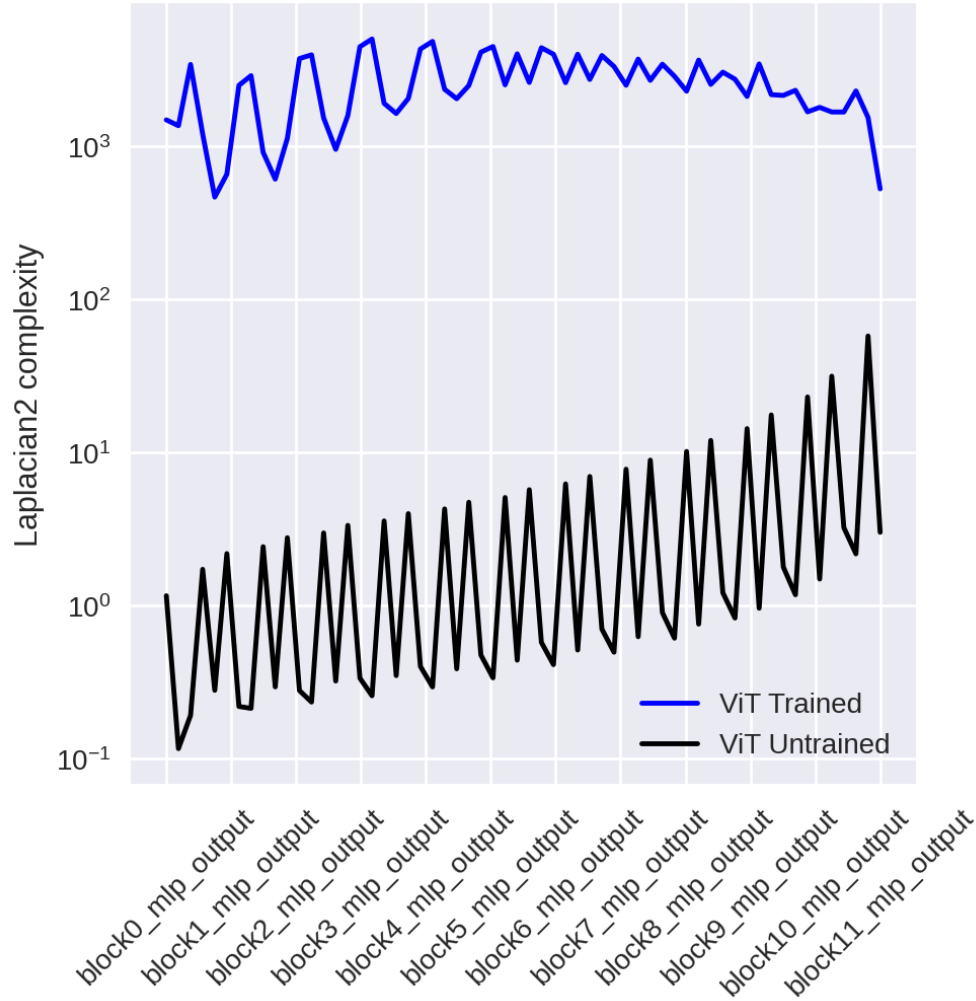


Figure 12: **Evolution of the high-frequency content in ViT with Laplace complexity.** We compute the high-frequency content along the depth of a ViT varying the weights, using Laplace2-operator. The curve represents the trained model, indicated by the blue curve, while the untrained model is represented by the black curve. Each point on the graph corresponds to a layer within the model. We show the labels representing the end of a block to give an idea of the evolution of the complexity inside a block.

## C Control conditions for the evidence of noise in the gradient

We add several control conditions on the experiment S3.2 to show the difference between an informative and uninformative gradient. We propose three different approaches :

- $\sigma = 0 \equiv \nabla_{\mathbf{x}}^{\sigma} \mathbf{f}(\mathbf{x}) = 0$  . In that case, we measure  $\|\mathbf{f}(\mathbf{x} + \epsilon) - \mathbf{f}(\mathbf{x})\|_2$
- $\nabla_{\mathbf{x}}^C \mathbf{f}(\mathbf{x}) = \rho(\nabla_{\mathbf{x}} \mathbf{f}(\mathbf{x}))$  where  $\rho$  represents the permutation operator. Here we destroy the spatial structure, and therefore the information represented by high and low frequencies.
- $\nabla_{\mathbf{x}}^C \mathbf{f}(\mathbf{x}) \sim \mathcal{U}(\min(\nabla_{\mathbf{x}} \mathbf{f}(\mathbf{x})), \max(\nabla_{\mathbf{x}} \mathbf{f}(\mathbf{x})))$ . Finally, we measure the information carried by some random noise, following a uniform distribution.

In the three cases, we compute the L2 norm between the first-order approximation of the model and something else containing no relevant information. We therefore expect a resulting curve with a higher estimation error than the others, containing some relevant information. We observe that is always the case for ResNet and ViT. This observation is a bit less clear for some radius value in the two first conditions on ConvNeXT but is present in the third condition.

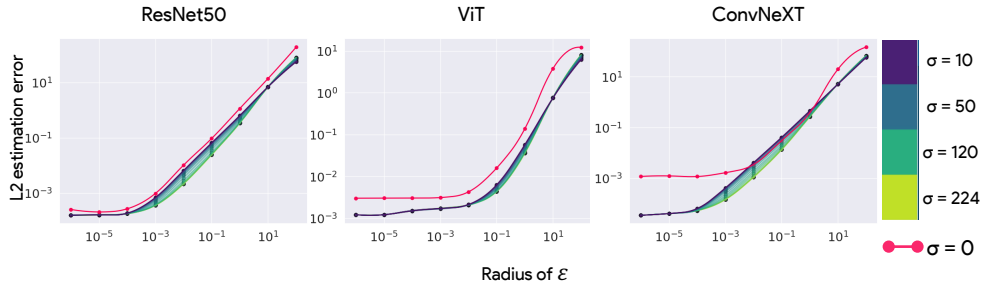


Figure 13: **Control condition**  $\sigma = 0$ . We plot the residual of the first-order approximation of the model, that is  $\mathbf{f}(\mathbf{x} + \epsilon) \approx \mathbf{f}(\mathbf{x}) + \epsilon \nabla_{\mathbf{x}} \mathbf{f}(\mathbf{x})$ , with the gradient  $\nabla \mathbf{f}$  filtered at different bandwidths  $\sigma$ . Additionally, we plot the control condition  $\sigma = 0$  in pink, representing the absence of information from the gradient.

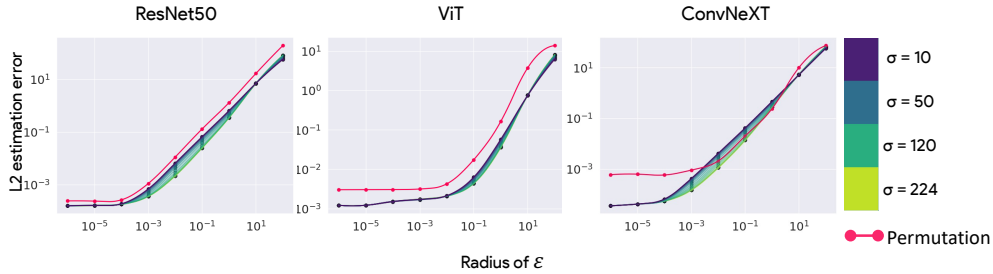


Figure 14: **Control condition**  $\nabla_{\mathbf{x}}^C \mathbf{f}(\mathbf{x}) = \rho(\nabla_{\mathbf{x}} \mathbf{f}(\mathbf{x}))$ . We plot the residual of the first-order approximation of the model, that is  $\mathbf{f}(\mathbf{x} + \epsilon) \approx \mathbf{f}(\mathbf{x}) + \epsilon \nabla_{\mathbf{x}} \mathbf{f}(\mathbf{x})$ , with the gradient  $\nabla \mathbf{f}$  filtered at different bandwidths  $\sigma$ . Additionally, we plot the control condition  $\nabla_{\mathbf{x}}^C \mathbf{f}(\mathbf{x}) = \rho(\nabla_{\mathbf{x}} \mathbf{f}(\mathbf{x}))$  in pink, representing some unstructured information from the gradient.

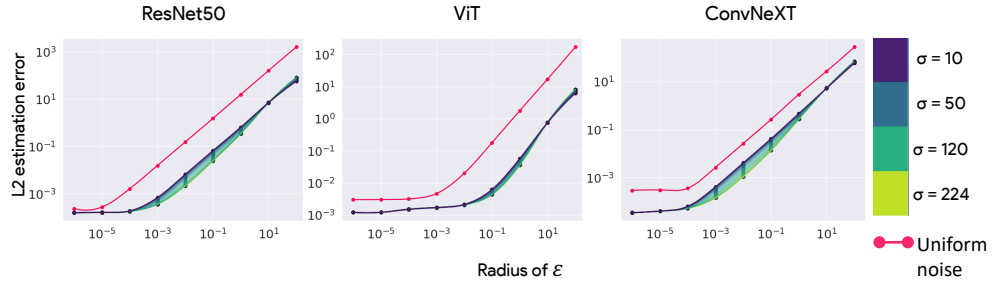


Figure 15: **Control condition**  $\nabla_x^C \mathbf{f}(\mathbf{x}) \sim \mathcal{U}(\min(\nabla_x \mathbf{f}(\mathbf{x})), \max(\nabla_x \mathbf{f}(\mathbf{x})))$ . We plot the residual of the first-order approximation of the model, that is  $\mathbf{f}(\mathbf{x} + \epsilon) \approx \mathbf{f}(\mathbf{x}) + \epsilon \nabla_x \mathbf{f}(\mathbf{x})$ , with the gradient  $\nabla \mathbf{f}$  filtered at different bandwidths  $\sigma$ . Additionally, we plot the control condition  $\nabla_x^C \mathbf{f}(\mathbf{x}) \sim \mathcal{U}(\min(\nabla_x \mathbf{f}(\mathbf{x})), \max(\nabla_x \mathbf{f}(\mathbf{x})))$  in pink, representing some random information from the gradient.